

The Influence of Solid State Diffusion on Microstructural Development During Solidification

J.N. DuPont

Department of Materials Science and Engineering
Lehigh University, Bethlehem, PA 18015
jnd1@lehigh.edu

Keywords: Solidification, solid state diffusion, microstructural development

Abstract. The primary factors that effect solid state diffusion during solidification are described and binary solute redistribution equations that permit estimation of the significance of solid state diffusion are discussed. Model calculations suggest that solid state diffusion of substitutional alloying elements in FCC alloys is insignificant under most processing conditions, while that of interstitial alloying elements is likely to be complete. Experimental data that supports these results are presented. Several cases that highlight the practical importance of microsegregation on performance of engineering alloys are described as well as methods for avoiding or minimizing microsegregation for improved properties. A solute redistribution model for handling the limiting cases of solute diffusion in ternary alloys is presented and model calculations are reviewed to reveal the strong influence diffusion can have on the solidification path and resultant microstructure.

Introduction

Solidification processing is used in a variety of fabrication methods such as casting, welding, laser surface treatment, and crystal growth. In many cases, products prepared from these processes are utilized in the as-solidified condition. In such applications, the mechanical properties and corrosion performance of the component are strongly influenced by the distribution of alloying elements and relative fraction of secondary constituents which form during the solidification process. It is often useful to make quantitative estimates of the resultant solidification microstructure as a means for controlling the ultimate component performance. The degree of solid state diffusion that occurs during solidification plays an important role in microstructural development. The objective of this article is to review factors that influence the extent of solid state diffusion that occurs during solidification, describe methods for estimating the expected degree of solid state diffusion, and discuss various models that can be used to account for the influence of solid state diffusion on the solidification path and resultant phase formation. Pertinent solute redistribution models for binary and ternary alloys will be described, and practical examples that highlight the importance of solid state diffusion will be provided.

Limiting Cases of Solute Redistribution in Binary Alloys

Many models have been developed in the solidification literature on solute redistribution and microstructural development in binary alloys that are capable of accounting for factors such as solid state diffusion, dendrite tip undercooling, and coarsening, and several review articles have been published on the subject [1-4]. While these models are quite useful, it is worth noting that most all conditions of solute redistribution in binary alloys must fall within two very simple cases: the lever law and so-called non-equilibrium Scheil equation [5]. Each of these conditions assumes that equilibrium is maintained at the solid/liquid interface, there is complete diffusion in the liquid, and there is no undercooling during nucleation or growth. The only difference between the two conditions is the assumption made about solid state diffusion – the lever law assumes solute diffusion is infinitely fast in the solid while the Scheil equation assumes diffusion is negligible. The relation between liquid composition and fraction liquid for equilibrium solidification is given simply by

$$C_L = \frac{C_o}{(1-k)f_L + k} \quad (1)$$

where C_L is the liquid composition at any value of fraction liquid, f_L , C_o is the nominal alloy composition, and k is the equilibrium distribution coefficient, defined as the ratio of solid to liquid compositions and assumed constant in Eq. 1. The corresponding relation between C_L and f_L for the Scheil condition is given by

$$C_L = C_o f_L^{(k-1)} \quad (2)$$

These two limiting cases of solute redistribution in binary alloys are quite useful as they allow the possible ranges of microstructural development to be easily bound. As an example, Fig. 1 shows the variation in liquid composition during solidification under equilibrium and non-equilibrium conditions for a 2 wt% B alloy from a binary eutectic system that exhibits linear solidus and liquidus lines, a k value of 0.2, and a eutectic composition of 20 wt% B. The solidification conditions and resultant microstructure under each extreme are quite different. Under equilibrium conditions, the liquid composition never becomes enriched to the eutectic composition because solute in the solid is uniformly distributed and therefore capable of dissolving all the solute before the eutectic point is reached in the liquid. Note from Eq. 1 that the maximum solute enrichment in the liquid for the equilibrium condition is given as C_o/k , which occurs when $f_L = 0$. In this case, $C_o/k < C_e$ (the eutectic composition). The resultant microstructure directly after solidification would simply consist of primary α with a uniform distribution of B. For the non-equilibrium case, Eq. 2 suggests that $C_L \rightarrow \infty$ as $f_L \rightarrow 0$ (for $k < 1$), which indicates the liquid composition will always become enriched to the eutectic point. This can be attributed to the lack of diffusion in the primary α phase, which leads to the inability of all the solute to be incorporated into the primary phase. Thus, directly below the eutectic temperature, the 2 wt% B alloy exhibits primary α with a concentration gradient and 0.06 weight fraction of the α/β eutectic when solidified under non-equilibrium conditions.

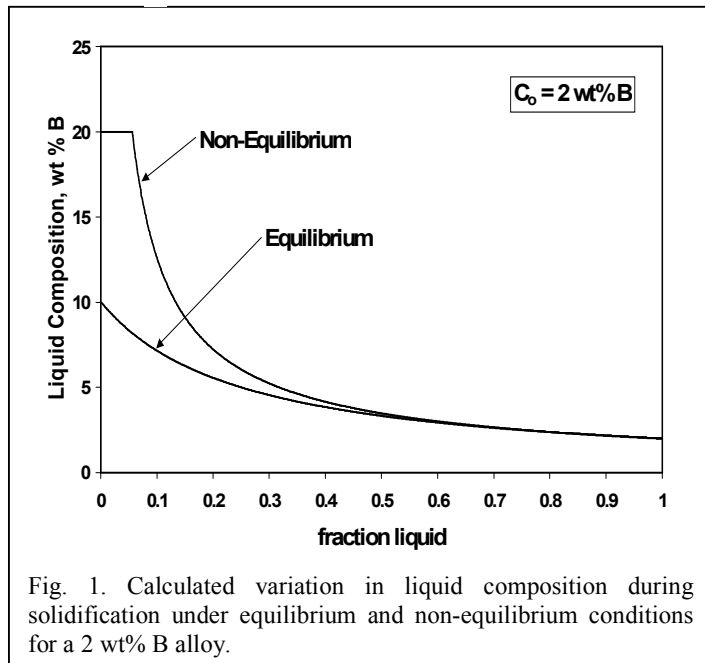


Fig. 1. Calculated variation in liquid composition during solidification under equilibrium and non-equilibrium conditions for a 2 wt% B alloy.

Estimating the Significance of Solid State Diffusion

Although the expressions described above are quite useful, they provide no insight into the possible role of solid state diffusion for a given solidification condition. Various solute redistribution equations have been developed over the years that account for solid state diffusion and can be used to estimate the significance of diffusion. Brody and Flemings [6] were the first to consider the influence of solid state diffusion on solute redistribution during solidification and, for the case of a linear growth rate, developed the following expression

$$C_s = kC_o \left[1 - \frac{f_s}{1 + \alpha k} \right]^{k-1} \quad (3)$$

Where C_s is the solid composition and f_s is the fraction solid. The α parameter in Eq. 3 is a dimensionless diffusion parameter defined as

$$\alpha = \frac{D_s t_f}{L^2} \quad (4)$$

Where D_s is the diffusivity of solute in the solid, t_f is the solidification time (time between the liquidus and terminal solidus), and L is half the dendrite arm spacing. The $D_s t_f$ term in the numerator essentially represents the distance the solute can diffuse in the solid during solidification, while the half dendrite arm spacing, L , represents the length of the concentration gradient. Thus, when $D_s t_f \ll L^2$, the solute is able to diffuse only a small fraction of the total gradient length and solid state diffusion will be insignificant. This represents the case in which $\alpha \approx 0$ and Eq. 3 reduces to the well-known Scheil equation. Thus, the dimensionless parameter in Eq. 4 is very useful for making initial estimates on the significance of back diffusion during solidification and warrants further consideration. The t_f and L terms will each depend on the cooling rate (ε) during solidification via

$$t_f = \frac{\Delta T}{\varepsilon} \quad (5)$$

$$L = \frac{\lambda}{2} = \frac{A \varepsilon^{-n}}{2} \quad (6)$$

Where ΔT is the solidification temperature range, λ is the dendrite spacing, and A and n are material constants. (Eq. 5 assumes a linear cooling rate through the solidification temperature range.) Thus, by knowing the solidification temperature range, cooling rate, and dendrite spacing-cooling rate relation, the α parameter can be directly estimated as a function of cooling rate and the potential influence of solid state diffusion can be determined. The value of n in Eq. 5 is typically between $\frac{1}{4}$ and $\frac{1}{3}$. For these two limiting cases, the expression for α is given by

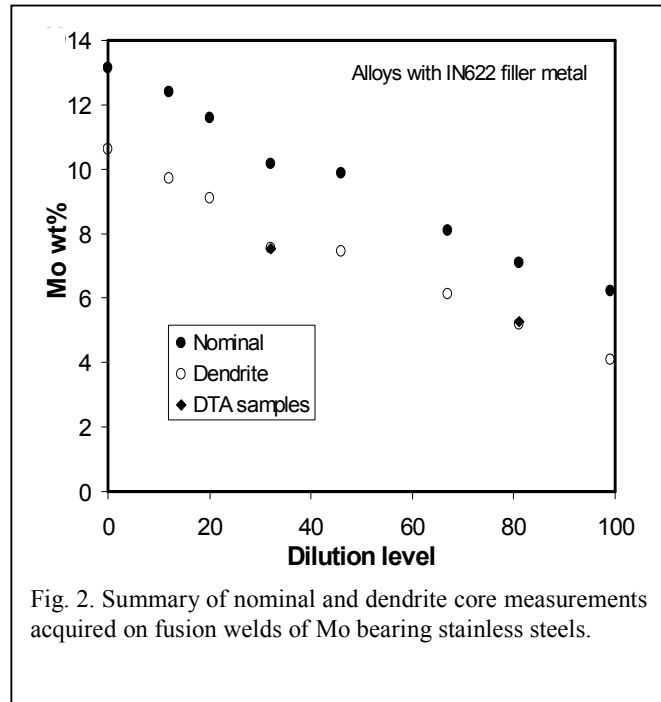


Fig. 2. Summary of nominal and dendrite core measurements acquired on fusion welds of Mo bearing stainless steels.

$$\alpha = \frac{4D_s \Delta T}{A} \quad \text{for } n = \frac{1}{2} \quad (7a)$$

$$\alpha = \frac{4D_s \Delta T}{A \varepsilon^{1/3}} \quad \text{for } n = \frac{1}{3} \quad (7b)$$

Eqs. 7 indicate that D_s and ΔT should have the strongest influence on solid state diffusion. Of these, D_s is the most important because it can change by orders of magnitude depending on temperature, host crystal structure, and the diffusion mechanism. Eqs. 7 also indicate that the cooling rate should have little or no effect on solid state diffusion during solidification. This can be understood by considering the competing effects the cooling rate has on the solidification time and dendrite arm spacing. Lower cooling rates will permit more time for back diffusion (Eq. 5), but the required diffusion distance also increases since the dendrite arm spacing increases (Eq. 6). These two opposing effects tend to offset each other so that there is often no significant effect from cooling rate. Experimental evidence is available to support this. Fig. 2 shows a summary of nominal and dendrite core measurements acquired on fusion weld made on a Mo bearing stainless steel with a Mo rich filler metal at various dilution levels [7]. These welds were solidified with cooling rates of ~ 300 °C/sec. The dendrite core compositions of several samples extracted from the fusion zone and re-solidified by differential thermal analysis (DTA) at 0.3 °C/sec are also shown. It is interesting to note that the core compositions are equivalent between samples solidified with cooling rates that differ by three orders of magnitude, providing verification that cooling rate has a negligible effect on the back diffusion potential under a wide range of cooling rates for this alloy system.

The results shown above and those from other studies have demonstrated that solid state diffusion during solidification is generally negligible for substitutional alloying elements in FCC materials such as nickel alloys and stainless steels [7,8]. This can be demonstrated by calculation of the α parameter for various alloying elements in FCC nickel as a function of cooling rate – Fig. 3. Here, upper bound values of α for each element were calculated by determining D_s at a representative liquidus temperature for many nickel alloys (~ 1350 °C [9,10]), using a large, but representative, value of ΔT of 200 °C, and reported values of $A = 32$ and $n = 0.31$ [11]. The values of A and n used here were for nickel base alloy 713. However, the values do not vary significantly among many nickel base alloys [12]. The α value decreases with increasing cooling rate due to the

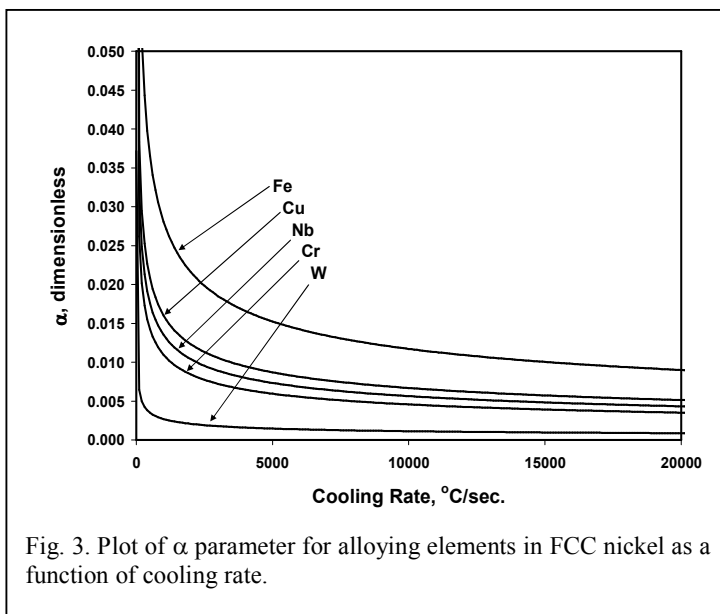
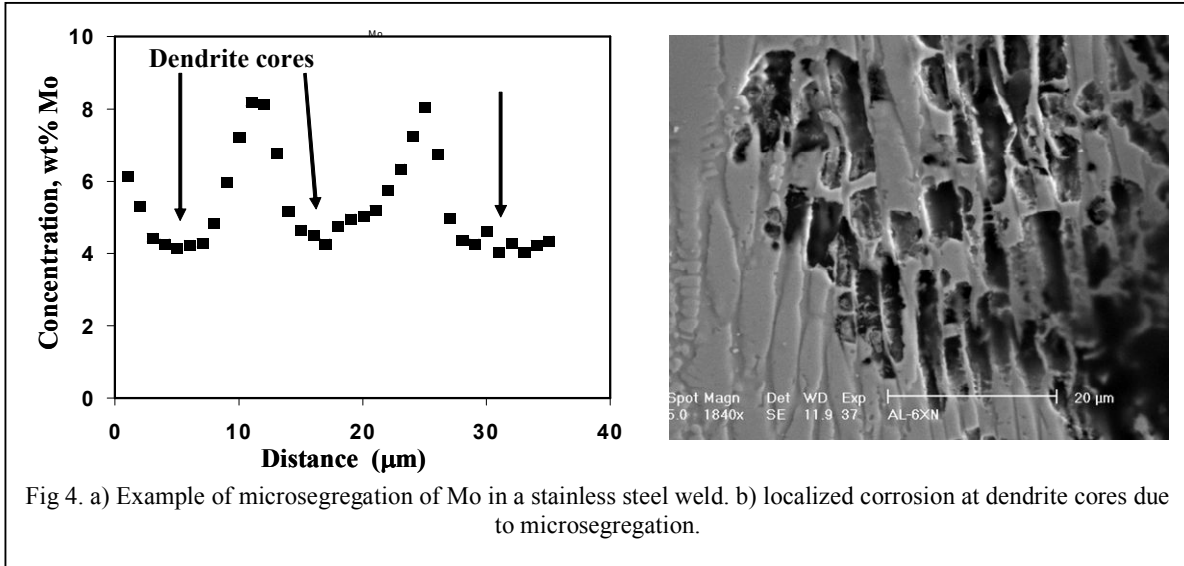


Fig. 3. Plot of α parameter for alloying elements in FCC nickel as a function of cooling rate.

decrease in solidification time (t_f) with increasing cooling rate. More importantly, note that $\alpha \ll 1$ for all the elements considered under all cooling rate conditions. Use of various values of ΔT , A , and n representative of other nickel base alloys does not change this result significantly. It is also important to note that an upper bound and constant value of D_s was calculated at a typical liquidus temperature of 1350 °C. The value of α can only decrease with the use of D_s values calculated at lower solidification temperatures. These results clearly demonstrate that solid state diffusion of substitutional alloying elements in nickel alloys is

insignificant during solidification for most processing conditions.

The limited diffusivity of alloying elements in nickel alloys and stainless steels often has important practical significance. Fig 4a shows an example of microsegregation of Mo in a stainless steel weld [7]. Although the nominal Mo concentration is 6 wt%, the core composition is only 4 wt% due to the inability for back diffusion. This leads to microsegregation-induced localized corrosion at the dendrite cores as shown in Fig. 4b. This problem limits the use of these materials in applications that require welded construction under conditions of aggressive corrosive environments [13]. Similar problems have been observed in nickel based weld overlay coatings that are used extensively in the power industry [14]. In those applications, preferential dendrite core corrosion has been found to initiate fatigue cracks that can lead to premature failure. Similarly, microsegregation in nickel base superalloys promotes uneven dissolution and coarsening of the γ' precipitates, which is the primary strengthening agent for these alloys [15].



It is interesting to note that the B-F solute redistribution model (Eq. 3) does not reduce to the lever law for conditions of equilibrium in which $\alpha \rightarrow \infty$. Clyne and Kurz [16] have shown that the mass balance used to derive the B-F equation is violated under conditions where diffusion becomes significant. Thus, the B-F model is only valid for conditions of moderate solid state diffusion. Noting that Eq. 3 reduces to the lever law for the limiting case of $\alpha = 0.5$, Clyne and Kurz proposed an alternate form for the α parameter that is defined as α' and given by

$$\alpha' = \alpha \left[1 - \exp\left(-\frac{1}{\alpha}\right) \right] - \frac{1}{2} \exp\left(-\frac{1}{2\alpha}\right) \quad (8)$$

This equation has the properties that $\alpha' \rightarrow 0$ as $\alpha \rightarrow 0$ and $\alpha' \rightarrow 0.5$ as $\alpha \rightarrow \infty$, thus causing the B-F model to conform to both the lever law and Scheil equation at the limiting cases of solute diffusion. Fig. 5 shows an example calculation of the B-F equation for C diffusion in a nickel alloy using the modified α' parameter and the temperature dependent diffusivity of C for a cooling rate of 650 °C/sec. Comparisons are made between the Scheil equation and lever law. These results indicate that the high rate of interstitial diffusion of C in FCC nickel permit direct use of the lever law. Lower cooling rate conditions should lead to the same conclusion (since α increases with decreasing cooling rate), and similar situations can be expected to exist for interstitial diffusion in BCC due to its lower packing factor and concomitant higher diffusion rates. Similarly, N diffusion in FCC and BCC alloys also probably obeys equilibrium behavior.

The higher diffusion rates of alloying elements in BCC alloys (compared to FCC alloys) can sometimes be used to eliminate or minimize problems associated with microsegregation. For example, Fe-Cr-Al overlay coatings have been developed [17] to replace nickel base superalloy weld overlay coatings that are susceptible to corrosion-fatigue that is initiated by localized corrosion at the alloy-depleted dendrite cores [14]. The composition of these alloys are adjusted so that the primary solidification phase is BCC ferrite. Fig. 6 shows an example of these coatings that exhibit a uniform distribution of Al and Cr, which is attributed to the high diffusion rate of Al and Cr in BCC Fe. A similar approach has recently been used to minimize microsegregation in stainless steels by control of the primary solidification phase [18].

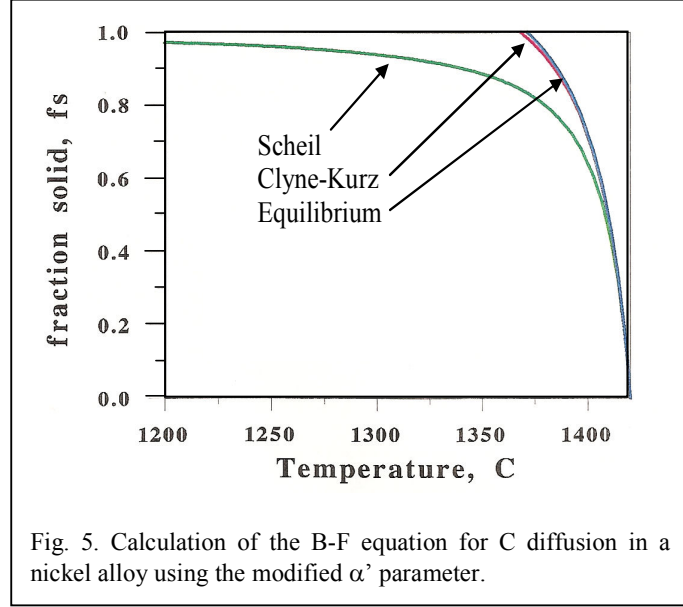


Fig. 5. Calculation of the B-F equation for C diffusion in a nickel alloy using the modified α' parameter.

Although the modified α parameter developed by Clyne and Kurz is useful, it should be noted that their analysis is not based on a physical interpretation of solid state diffusion during solidification. More recently, Kobayashi [19] has developed an exact solution to the solute redistribution problem in binary alloys that accurately accounts for solid state diffusion. Although a numerical method is required for a complete analysis, an approximate solution to the problem is available and, for a planar geometry, is given by

$$C_s = kC_o \xi^{\frac{k-1}{1-\beta k}} \left\{ 1 + \Gamma \left[\frac{1}{2} \left(\frac{1}{\xi^2} - 1 \right) - 2 \left(\frac{1}{\xi} - 1 \right) - \ln \xi \right] \right\} \quad (9)$$

Where:

$$\beta = \frac{4\alpha}{1+4\alpha}; \quad \xi = 1 - (1 - \beta k) f_s; \quad \Gamma = \frac{\beta^3 k(k-1)((1+\beta)k-2)}{8\alpha(1-\beta k)^3} \quad (10)$$

This solution covers the full range of diffusion behavior. For example, when $D_s = 0$, then $\gamma = \beta = \Gamma = 0$, $\xi = 1 - f_s$, and Eq. 9 reduces to the Scheil equation. Similarly, for $D_s \rightarrow \infty$ the equilibrium lever law can be obtained. More recently, Yeum *et al.* [20] have extended these concepts to develop an accurate finite difference method for estimating the significance of back-diffusion during solidification.

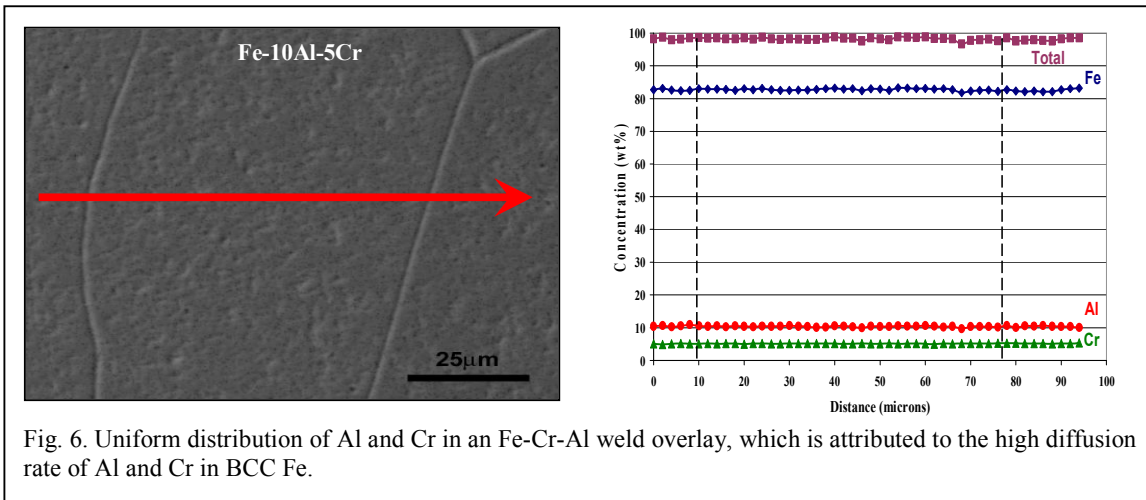


Fig. 6. Uniform distribution of Al and Cr in an Fe-Cr-Al weld overlay, which is attributed to the high diffusion rate of Al and Cr in BCC Fe.

Ternary Alloys

The influence of solid state diffusion on the solidification path and resultant microstructure of ternary alloys is considerably more complex because the behavior of two solutes must now be considered. As an example, Fig. 7 schematically shows the C-rich corner of the liquidus surface for an A-B-C ternary eutectic system which exhibits three primary solidification phases: α , β , and γ . An alloy with a nominal composition located in the C-rich corner could potentially exhibit six different solidification paths. In Fig. 7a, the liquid composition is never enriched to either the α/β or α/γ mono-variant eutectic line. The microstructure developed under this solidification path would simply consist of primary α . This is similar to equilibrium solidification of a binary alloy which has a nominal composition below the maximum solid solubility. In Figs. 7b and 7c, the liquid composition is enriched to the point where the primary solidification path intersects the mono-variant eutectic line separating the α and β phases. The solidification path then follows the eutectic line as the α and β phases form simultaneously from the liquid by a mono-variant eutectic reaction. Depending on the diffusivity of A and B in the solid [21], solidification could be completed along the eutectic line (Fig. 7b), or the liquid composition could be enriched all the way to the ternary eutectic composition (Fig. 7c) at which point the ternary $\alpha/\beta/\gamma$ eutectic constituent will form isothermally. For the case shown in Fig. 7b, the microstructure will contain the α primary phase and the binary type α/β eutectic constituent. The microstructure formed from the solidification path shown in Fig. 7c will exhibit primary α , the eutectic type α/β constituent, and the $\alpha/\beta/\gamma$ ternary eutectic.

In Figs. 7d and 7e, the primary solidification path is oriented such that it intersects the α/γ mono-variant eutectic line instead of the α/β line. This could occur if the diffusivity of B in α is very low (relative to element A) and/or the solubility of B in α is low (i.e., low k), which would cause the liquid to become highly enriched in B during solidification. The solidification path will then follow the mono-variant eutectic line as the α and γ phases form simultaneously from the liquid by a mono-variant eutectic reaction. Depending on the diffusivity of A and B in the solid, solidification could be completed along the α/γ eutectic line (Fig. 7d), or the liquid composition could be enriched all the way to the ternary eutectic (Fig. 7e) at which point the ternary $\alpha/\beta/\gamma$ eutectic constituent will form isothermally. Finally, Fig. 7f demonstrates the case in which the primary solidification path directly intersects the $\alpha/\beta/\gamma$ ternary eutectic point. In this case, the as-solidified microstructure would exhibit primary α and the ternary $\alpha/\beta/\gamma$ ternary eutectic constituent.

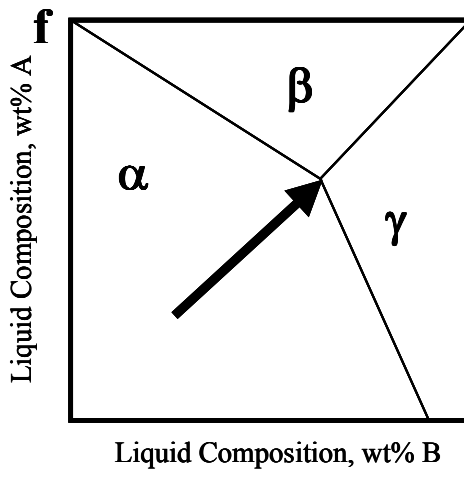
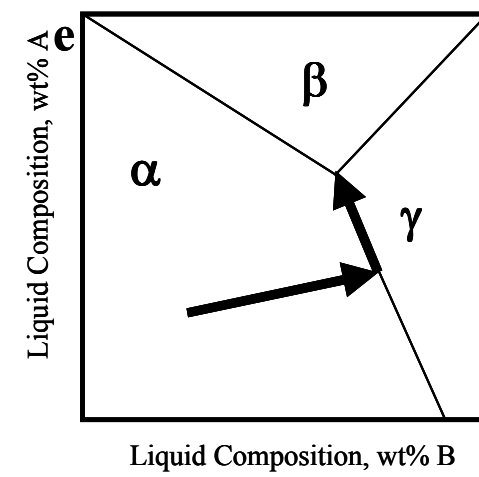
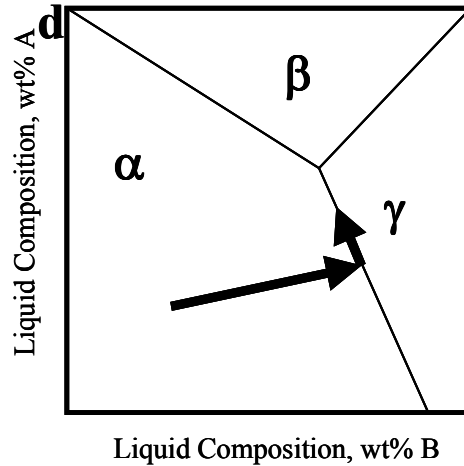
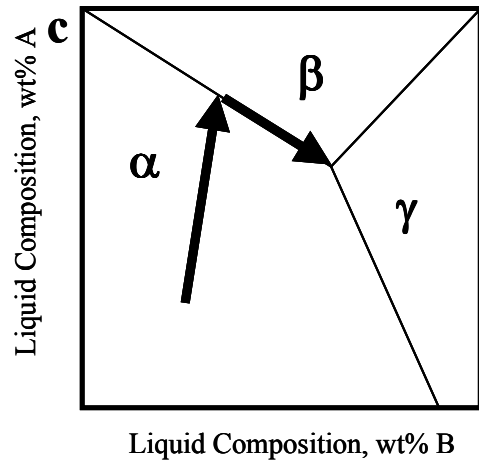
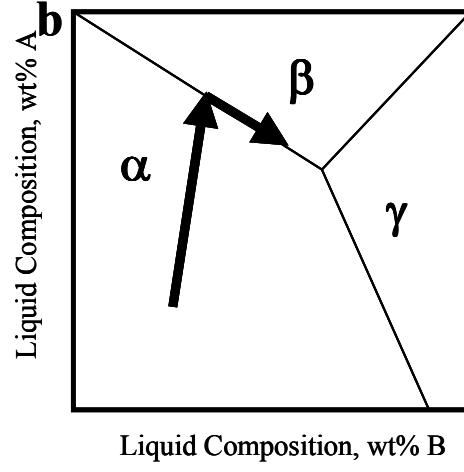
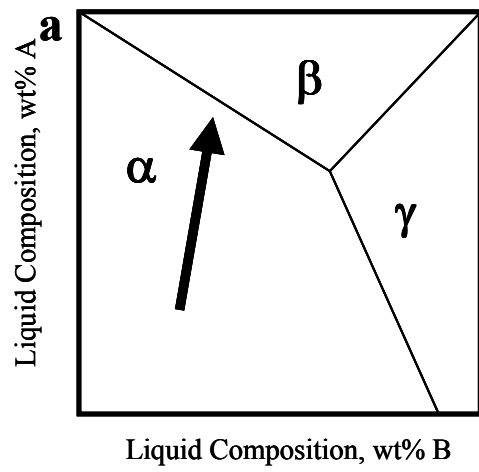


Fig. 7. Schematic illustration of six potential solidification paths of a C rich ternary alloy.

These examples illustrate the difficulty in making simple quantitative estimates of solidification paths and resultant microstructures in ternary alloys. For ternary solidification, three limiting cases can be identified based on the diffusivity of solute in the solid phases: 1) negligible diffusion of each solute in the solid phases, referred to as non-equilibrium solidification, 2) negligible diffusion of one solute in the solid phases and infinitely fast diffusion of the other solute in the solid phases, referred to here as intermediate equilibrium, and 3) infinite diffusion of each solute in the solid phases (equilibrium). The pertinent solute redistribution equations that describe these three conditions have recently been developed [22]. The analysis involves two sets of expressions for each condition – one to describe the solidification path during primary solidification, and a second set to describe solute redistribution along the mono-variant eutectic lines. Simple closed form solutions can be obtained for the primary solidification paths, which are given by

$$\text{Equilibrium:} \quad C_{LA} = \frac{C_{oA}}{\left(\frac{1-k_{\alpha A}}{1-k_{\alpha B}}\right)\left(\frac{C_{oB}-k_{\alpha B}C_{LB}}{C_{LB}}\right) + k_{\alpha A}} \quad (11a)$$

$$\text{Intermediate Equilibrium:} \quad C_{LA} = C_{oA} \left(\frac{C_{oB}-k_{\alpha B}C_{LB}}{(1-k_{\alpha B})C_{LB}}\right)^{k_{\alpha A}-1} \quad (11b)$$

$$\text{Non-Equilibrium:} \quad C_{LA} = C_{oA} \left(\frac{C_{LB}}{C_{oB}}\right)^{\frac{k_{\alpha A}-1}{k_{\alpha B}-1}} \quad (11c)$$

Where C_{Li} is the concentration of element i in the liquid, C_{oi} is the nominal concentration of element i , and $k_{\alpha i}$ is the equilibrium distribution coefficient for element i between the liquid and primary α phase. Eqs. 11 describe the solidification path for primary solidification that can be plotted directly on the liquidus surface. The plot is initiated at $C_{LA} = C_{oA}$ and $C_{LB} = C_{oB}$. If the value of $k_{\alpha B} < 1$, then solute is rejected from the solid to the liquid and C_{LB} will increase during solidification. In this case, the value of C_{LB} is repeatedly increased by some small amount ΔC_{LB} and the corresponding value of C_{LA} is determined through Eqs. 11 to trace out the primary solidification path. If the value of $k_{\alpha B} > 1$, then the solid becomes enriched in solute while the liquid becomes depleted in solute so that C_{LB} will decrease during solidification. In this case, the value of C_{LB} is repeatedly reduced by some small amount ΔC_{LB} and the corresponding value of C_{LA} is calculated. Besides the assumptions described above for solid state diffusion, these expressions assume infinite diffusion of each solute in the liquid phase, equilibrium at the solid/liquid interface, no undercooling during growth, constant equilibrium distribution coefficients, and that solute redistribution of each element occurs independently. Expressions for solute redistribution along the mono-variant eutectic line must be solved by a numerical technique as described elsewhere [22].

Fig. 8 shows example calculations of the primary solidification paths for a hypothetical 5wt%A-10wt%B alloy in which $k_{\alpha A} = 0.5$ and $k_{\alpha B} = 0.7$. The ternary system exhibits a eutectic point at $C_{LA} = 15$ wt% A and $C_{LB} = 15$ wt% B. In Fig. 8, the position of the nominal alloy composition causes the non-equilibrium and intermediate equilibrium primary solidification paths to straddle the ternary eutectic point so that different mono-variant eutectic reactions occur. Three significantly different results are obtained for each condition.

The equilibrium primary path does not reach a eutectic line so that the weight fraction of primary phase (f_{α}^p) is unity and the fraction of α/β eutectic ($f_{\alpha/\beta}$) and $\alpha/\beta/\gamma$ eutectic ($f_{\alpha/\beta/\gamma}$) is zero, i.e., $f_{\alpha}^p = 1$ and $f_{\alpha/\beta} = f_{\alpha/\beta/\gamma} = 0$. The intermediate equilibrium primary path intersects the $L \rightarrow (\alpha +$

β) reaction line, but the liquid is completely consumed along this line so that $f_{\alpha}^p = 0.91$, $f_{\alpha\beta} = 0.09$, and $f_{\alpha/\beta/\gamma} = 0$. Finally, the non-equilibrium case intersects the $L \rightarrow (\alpha + \gamma)$ line so that the α/γ eutectic forms instead of the α/β eutectic, and the liquid composition is enriched to the ternary eutectic point with the final result of $f_{\alpha}^p = 0.8$, $f_{\alpha/\gamma} = 0.1$, and $f_{\alpha/\beta/\gamma} = 0.1$.

It is interesting to note that these results for ternary solidification show similarities to the companion binary cases. For example, a ternary eutectic alloy solidifying under equilibrium conditions will only exhibit the mono-variant eutectic reaction when the nominal alloy concentration is above the maximum solid solubility. This result is similar to the binary case, in which the invariant $L \rightarrow (\alpha + \beta)$ eutectic reaction only occurs when the nominal composition is greater than the maximum solid solubility. For a ternary eutectic alloy solidifying under non-equilibrium conditions, the liquid is always enriched to a terminal invariant point so that both the mono-variant and invariant ternary eutectic reactions are always expected to occur. This case is similar to the binary non-equilibrium Scheil condition in which the liquid is always enriched to the invariant $L \rightarrow (\alpha + \beta)$ eutectic reaction, regardless of the nominal composition. The intermediate equilibrium condition lies between the equilibrium and non-equilibrium conditions in which a

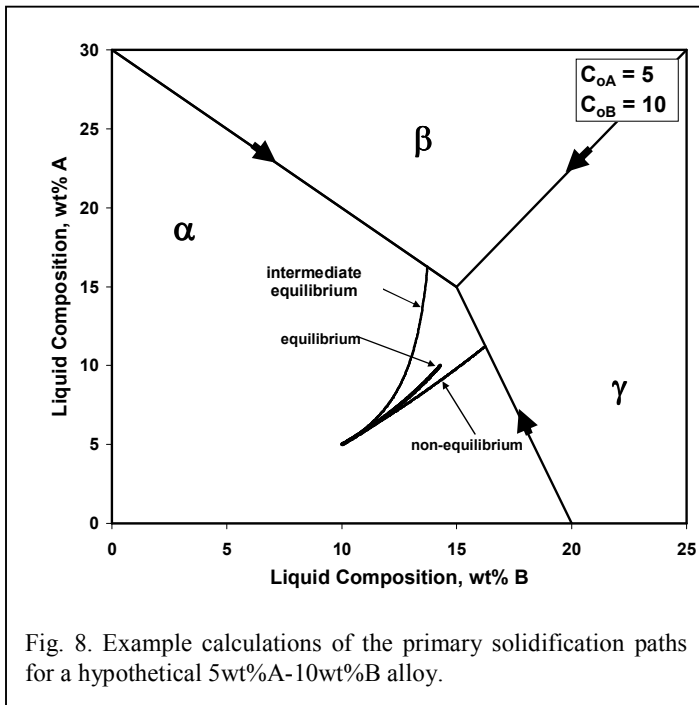


Fig. 8. Example calculations of the primary solidification paths for a hypothetical 5wt%A-10wt%B alloy.

mono-variant eutectic reaction is always expected to occur, but solidification can terminate before the invariant ternary eutectic reaction is reached.

These expressions are useful for estimating solute redistribution behavior and resultant solidification microstructures in ternary alloys and can also be used to model multi-component alloys when two solutes dominate the microstructural evolution process. This approach has been used on nickel base superalloys in which segregation and the resultant phase formation is dominated by the presence of Nb and C that follow the intermediate equilibrium condition (i.e, equilibrium conditions for C, Scheil condition for Nb) [21]. In this case, small variations in alloy composition that have a significant effect on the

solidification behavior can be understood and controlled by combining the solute redistribution equations with calculated liquidus projections. An example of this for the multi-component commercial superalloy IN718 is shown in Table 1, which lists the chemical composition of five different heats of IN718 that contain variations in the Nb and C concentrations and the measured start temperature of the $L \rightarrow \gamma + \text{NbC}$ reaction for each alloy. Note that a seemingly small change in C content from 0.04 to 0.09 wt% increases the $L \rightarrow \gamma + \text{NbC}$ start temperature by an average of ~ 36 $^{\circ}\text{C}$.

Fig. 9 shows calculated primary solidification paths (as calculated with Eq. 11b) of five different heats of IN718 plotted on the IN718 calculated liquidus projection. The liquidus projection was computed by determining the position of the mono-variant eutectic lines that separate the γ , NbC, and Laves primary phase fields. Although the diagram is displayed in ternary-like fashion, it accounts for the presence of eight elements (Ni-Fe-Cr-Mo-Al-Ti-Nb-C) by approximating " γ " as an elemental constituent. The liquid composition at which the $L \rightarrow \gamma + \text{NbC}$ reaction is replaced by $L \rightarrow \gamma + \text{Laves}$ is calculated at 19.1 wt% Nb and 0.03 wt% C. These values are in excellent agreement with those previously reported as 19.1 wt% Nb and 0.04 wt% C [10]. The intersection of the

primary solidification path with the γ /NbC eutectic line provides a predicted value for the start temperature of the $L \rightarrow \gamma + \text{NbC}$ reaction. These predicted values are noted in Fig. 9 and summarized in Table 1, and good agreement is observed between the calculated and measured reaction temperatures.

Table 1. Chemical composition along with measured and calculated $L \rightarrow \gamma + \text{NbC}$ temperatures for five different heats of Alloy IN718.

Element	Heat 1	Heat 2	Heat 3	Heat 4	Heat 5
Ni	Bal.	Bal.	Bal.	Bal.	Bal.
Al	0.46	0.41	0.28	0.46	0.42
Cr	17.65	17.15	17.68	17.32	17.19
Fe	19.36	20.56	19.47	19.49	19.19
Mo	2.90	2.92	2.87	2.88	2.86
Nb	5.17	5.02	2.97	6.38	5.07
Ti	0.90	0.87	0.84	0.88	0.90
C	0.04	0.02	0.05	0.06	0.09
Measured $L \rightarrow \gamma + \text{NbC}$ Temperature, °C	1260 ± 12	Not Detected	1290 ± 9	1283 ± 9	1296 ± 9
Calculated $L \rightarrow \gamma + \text{NbC}$ Temperature, °C	1260	1237	1297	1264	1294

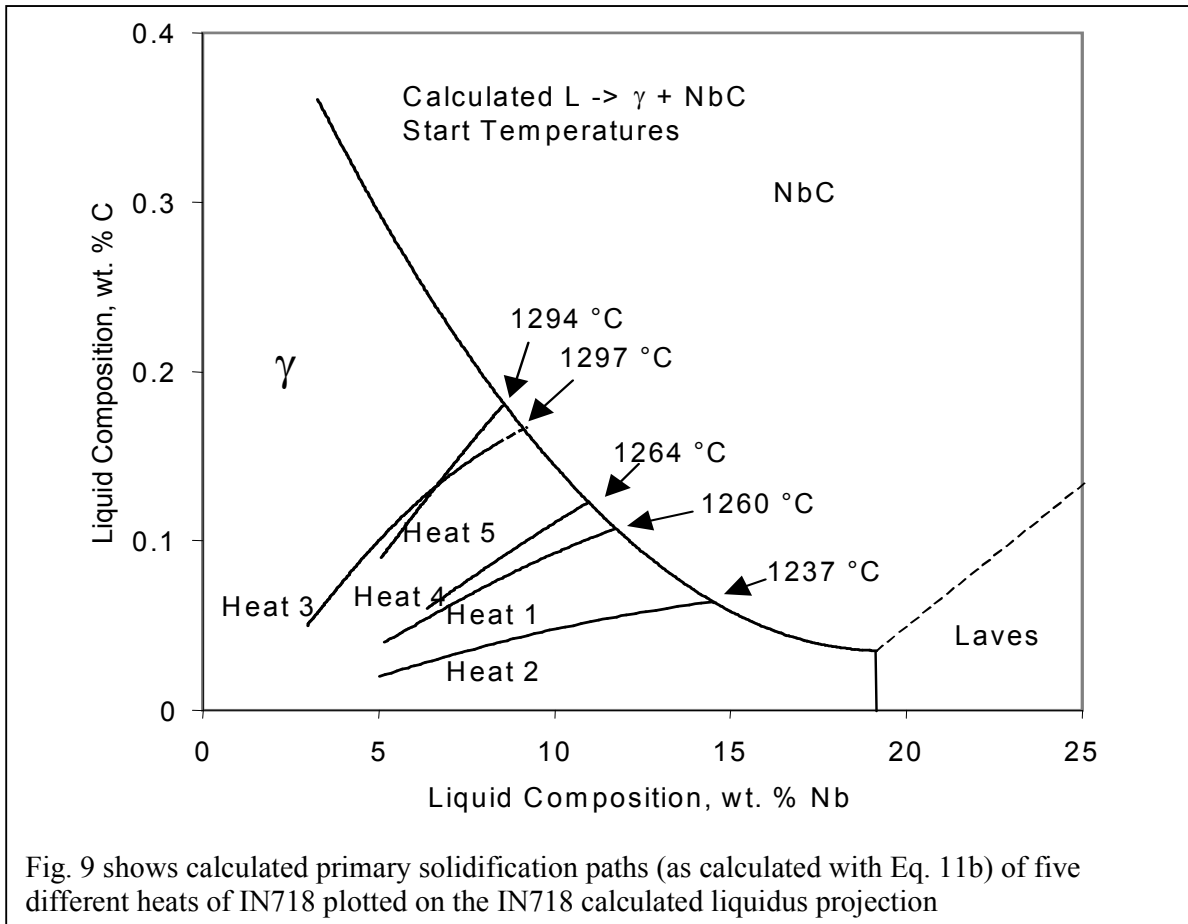


Fig. 9 shows calculated primary solidification paths (as calculated with Eq. 11b) of five different heats of IN718 plotted on the IN718 calculated liquidus projection

Summary and Future Directions

The results presented above demonstrate the strong influence solid state diffusion can have on the solidification path and resultant microstructure. The information available to date supports the view that solid state diffusion of substitutional alloying elements in FCC alloys is insignificant under most processing conditions, while that of interstitial elements is likely to be complete. Problems associated with microsegregation due to limited solid state diffusivity can often be surmounted by adjusting the alloy composition to promote solidification of a primary phase with enhanced diffusivity. This approach has been successfully applied to stainless steels and ferritic Fe-Cr-Al weld overlay coatings. The influence of solid state diffusion in binary alloys can be handled quite accurately with available solute redistribution equations, and models are available to handle the limiting cases of solute diffusion in ternary alloys. Future efforts should be dedicated to further verification of newer computational software codes that could be used for microstructural prediction in multi-component alloys [23,24]. These codes are useful because they often permit variations in partition coefficients, solid and liquid diffusivities, and phase boundary positions during solidification. Although these abilities are certainly useful for design of practical engineering alloys that can contain over ten alloying elements, detailed experimental validation is often required to account for differences observed between experimental and calculated results. In view of this, the approaches presented here can often be combined with calculated phase diagram information in order to evaluate the influence of each parameter (e.g., solid state diffusion behavior, k values, phase boundary positions) on solidification behavior and resultant microstructure. This approach is often very useful for modeling multi-component alloys in a straight forward manner using a binary or ternary analog and for identifying sources of inaccuracies when results from software codes do not match experimental results [21,25].

References

1. W.J. Boettinger, S.R. Coriell, A.L Greer, A. Karma, W. Kurz, M. Rappaz, and R. Trivedi, *Acta Materialia*, 2000; 48: p. 43.
2. R. Trivedi and W. Kurz, *International Materials Reviews*, 1994; 39: p. 49.
3. V. Laxmanan, *Acta Materialia*, 1985; 33: p. 1023.
4. T.P. Battle, *International Materials Reviews*, 1992; 37: p. 249
5. E. Scheil, *Z Metallk*, 1942; 34: p. 70
6. H.D. Brody and M.C. Flemings, *Transactions of AIME*, 1966; 236: p. 615
7. S.W. Banovic, J.N. DuPont, and A.R. Marder, *Science & Technology of Welding and Joining*, 2003; 6: p. 374.
8. J.N. DuPont, C.V. Robino, and A.R. Marder, *Metallurgical and Material Transactions A*, 1998; 29A: p. 2797.
9. M.J. Cieslak, T.J. Headley, T. Kollie, and A.D. Romig, *Metallurgical Transactions A*, 1988, 19: p. 2319.
10. J.N. DuPont, C.V. Robino, A.R. Marder, M.R. Notis, and J.R. Michael, *Metallurgical and Material Transactions A*, 1988; 29: p. 2785.
11. H. Joo, and H. Takeuchi, *Tokai Daigaku Kiyo*, 1994; 34: p. 203.
12. U. Heubner, M.Kohler, and B. Prinz, *Superalloys 1988*, 1988, ASM International, Materials Park, OH, pp. 437.
13. A. Garner, *Metal Progress*, 1985, April, p. 31.
14. K.R. Luer, J.N. DuPont, A.R. Marder, and C.K. Skelonis, *Materials at High Temperatures*, 2001; 18: p. 11.
15. R. Rosenthal and D.R.F. West, *Materials Science and Technology*, 1999; 15: p. 1387.
16. T.W. Clyne and W. Kurz, *Metallurgical Transactions A*, 1981; 12A: p. 965
17. S.W. Banovic, J.N. DuPont, and A.R. Marder, *Welding Journal*, 1999; 78: p. 23s.
18. T.D. Anderson, M.J. Perricone, J.N. DuPont, A.R. Marder, Phase Transformations and Microstructural Evolution of Mo-bearing Stainless Steels, accepted for publication in *Metallurgical and Materials Transactions A*

19. S. Kobayashi, *Journal of Crystal Growth*, 1988; 88: p. 87
20. K.S. Yeum, V. Laxmanan, and D.R. Poirier, *Metallurgical and Materials Transactions A*, 20:p.2847.
21. J.N. DuPont, C.V. Robino, and A.R. Marder, *Acta Materialia*, 1998, 46; p. 4781.
22. J.N. DuPont, *Metallurgical and Materials Transactions A*, 2006, 37: p. 1937.
23. Saunders, N. 2001, *Fe-Data Thermodynamic Database 3.0*, Thermotech, Ltd., The Surrey Research Park, Guildford, UK, Thermotech, Ltd.
24. Sundman, B. 2001, *Thermo-Calc. S-100 44[N].*, Thermotech, Ltd., The Surrey Research Park, Stockholm, Sweden.
25. M.J. Perricone and J.N. DuPont, *Metallurgical and Materials Transactions A*, 2006; 37, p. 1267.